Simultaneous Precision Gravimetry and Magnetic Gradiometry with a Bose-Einstein Condensate: A High Precision, Quantum Sensor

K. S. Hardman,* P. J. Everitt, G. D. McDonald, P. Manju, P. B. Wigley, M. A. Sooriyabandara, C. C. N. Kuhn, J. E. Debs, J. D. Close, and N. P. Robins

Quantum Sensors and Atomlaser Lab, Department of Quantum Science, Australian National University, Canberra 0200, Australia

(Received 8 March 2016; published 21 September 2016)

A Bose-Einstein condensate is used as an atomic source for a high precision sensor. A 5×10^6 atom $F = 1$ spinor condensate of ^{87}Rb is released into free fall for up to 750 ms and probed with a $T = 130$ ms Mach-Zehnder atom interferometer based on Bragg transitions. The Bragg interferometer simultaneously addresses the three magnetic states $|m_f = 1, 0, -1\rangle$, facilitating a simultaneous measurement of the acceleration due to gravity with a 1000 run precision of $\Delta g/g = 1.45 \times 10^{-9}$ and the magnetic field gradient to a precision of 120 pT/m.

DOI: 10.1103/PhysRevLett.117.138501

Acquiring accurate and precise data on magnetic and gravity fields is critical to progress in mineral discovery [1,2], navigation [3], and climate science [4]. A diverse array of tools and techniques have been developed to improve the quality of measurements, including macroscopic classical springs [5], falling corner cubes [6], and solid-state [7] and superconducting [8] systems. Following the early pioneering work in precision atom interferometry [9], the past decade has seen devices using cold atomic sources become competitive with traditional acceleration sensors [10–14]. Technical developments improving size, weight, and power have allowed for applications in space science [15] and field ready state-of-the-art gravimeters and gradiometers [16–18].

Like their classical counterparts, sensors based on cold atoms measure the trajectory of the test particles [19]. Unlike classical particles, atoms offer internal degrees of freedom, allowing for the possibility of additional simultaneous measurements including time, magnetic fields, and magnetic field gradients. Although these advantages are intrinsic to all atomic sources, ultracold Bose-Einstein condensates (BECs) offer additional benefits over thermal atoms. An intrinsic feature of a BEC is a spatial coherence equivalent to the size of the cloud, which is generally hundreds of microns, while thermal sources have a spatial coherence length on the order of the de Broglie wavelength, $\lambda_{\mathrm{dB}} = \sqrt{2\pi\hbar^2/mk_BT}$ ($\sim$0.1 μm). This spatial coherence has been shown to provide a robustness to systematics which results in the loss of fringe contrast, such as cloud mismatch at the final beam splitter pulse [20]. The BEC then allows a sensor to be operated unshielded in varying environments where background field gradients and curvatures are non-negligible.

This Letter introduces a new type of sensor which *simultaneously* measures gravity and magnetic field gradients to high precision. In this lab-based sensor, an optically trapped cloud of ^{87}Rb atoms is cooled to condensation and projected into an $F = 1$ spin superposition, then passed through a vertical light pulse Mach-Zehnder interferometer based on Bragg transitions [21,22]. The spin superposition, in combination with the large spatial coherence of the BEC, allows simultaneous precision measurement of gravity and an absolute magnetic field gradient in an unshielded device [23]. A 2×10^6 atom condensate is used in the interferometer [24] with no loss in contrast over all interferometer times.

The experimental schematic is shown in Fig. 1. A hot sample of ^{87}Rb atoms is created and precooled in a 2D magneto-optical trap (MOT). These precooled atoms are transferred to an aluminum ultrahigh vacuum cell via a high impedance gas flow line and a blue detuned push beam. In 6 s, 5×10^9 atoms are collected in a 3D MOT where a standard compression and polarization gradient cooling sequence is applied achieving a 20 μK temperature. The atoms are then loaded into a hybrid magnetic quadropole and a crossed optical dipole trap. An initial stage of evaporation is completed using a microwave knife over 4.5 s, leaving 4×10^7 atoms at 4 μK and a phase space density of 1×10^{-4}. The magnetic field gradient is decreased from 150 to 25 G/cm over 200 ms, where the atoms are no longer supported against gravity. This efficiently loads all the atoms into a crossed dipole trap. The magnetic field is subsequently reduced to zero and extinguished. A pair of 1070 nm broad linewidth fiber lasers intersecting at 22.5° each, with beam waists of 300 μm, provide the optical trap volume. Forced evaporation is then completed by simultaneously reducing the intensity of both optical beams. After 2 s of evaporation, a pure $|F = 1, m_f = -1\rangle$ 2×10^6 atom condensate is formed with an in trap width of $\sim$50 μm. The effective thermal

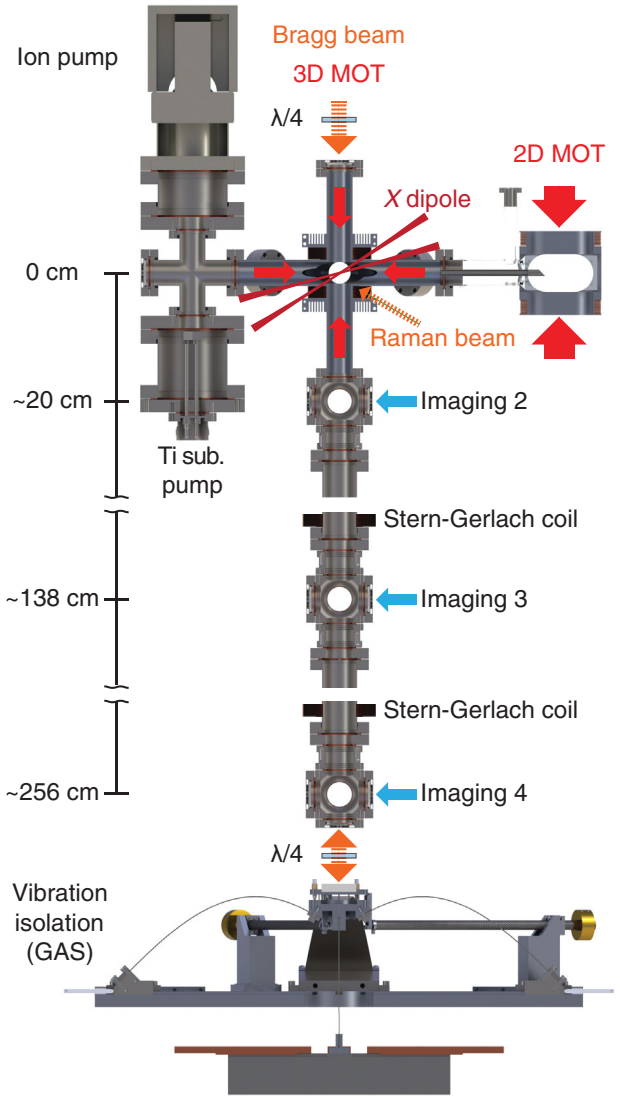

FIG. 1. Overview of the experimental setup.

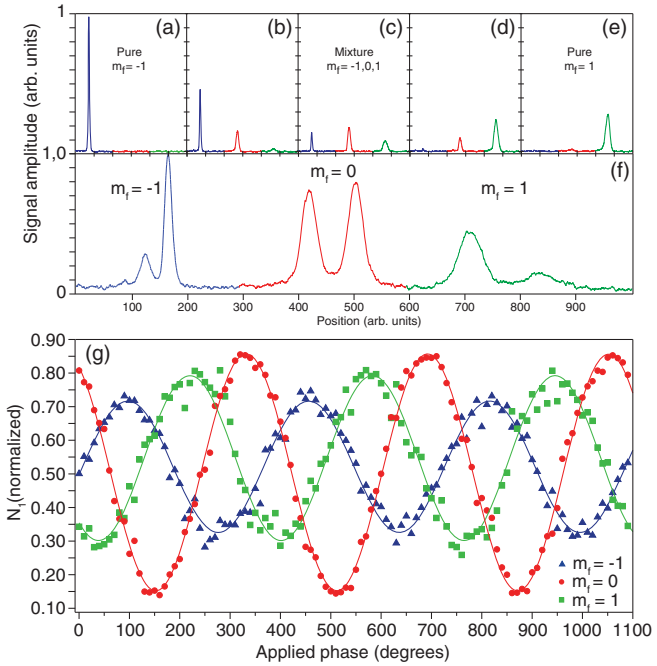

FIG. 2. (a)–(e) By adjusting Raman pumping power, it is possible to produce pure (a) $|m_f = -1\rangle$ or (e) $|m_f = 1\rangle$ or any spin mixture condensate. A Stern-Gerlach pulse separates the states before imaging. The variation in cloud profile is due to magnetic lensing from curvature in the Stern-Gerlach field. (f) A typical FMI image of a three state interferometer. (g) The interference fringes produced by a $T = 60$ ms Mach-Zehnder interferometer with a spinor BEC source achieving 9 mrad phase noise in 100 runs. Changes in local gravity are monitored through correlated phase shifts of all m_f states. The absolute background field, B, and the field gradients, dB/dz, are found from the relative phase shifts between all of the states ($\Delta\Phi_{-1}$, $\Delta\Phi_1$, and $\Delta\Phi_{-1} + \Delta\Phi_1$) using Eq. (1). Changes in dB/dz are monitored through anticorrelated phase shifts of $|m_f = -1\rangle$ and $|m_f = 1\rangle$ relative to $|m_f = 0\rangle$.

temperature of the condensate is estimated to be significantly below 50 nK for an up to 750 ms expansion. Controlling the final trap depth allows for the creation of a pure BEC or ultracold thermal source. Following production of the condensate, the optical trap is extinguished suddenly ($\sim 10\ \mu$s) and the atoms fall under gravity. The apparatus allows for a 750 ms TOF, with four regions available for horizontal imaging at 0–25, 220, 530, and 750 ms. Standard absorption imaging techniques are used for the 0–25 and 220 ms imaging regions. Frequency modulation imaging (FMI) [25,26] is implemented for the 530 and 750 ms drop times used for high sensitivity interferometers.

A pair of far detuned, copropagating, mutually linear polarized beams are pulsed on 5 ms after the atoms are released from the optical trap to induce Raman transitions. These transfer the condensate into a magnetic superposition state of $|m_f = 1, 0, -1\rangle$; see Figs. 2(a)–2(e). The Raman beams are aligned through mutual fiber coupling that ensures a negligible relative angle. A vertically oriented Mach-Zehnder atom interferometer consisting of three 30 GHz detuned Bragg pulses (ensuring orthogonal internal m_f states) is used to measure the phase accumulated on all three internal states as they fall. The Bragg lattice is generated by two frequency shifted beams with orthogonal linear polarizations. These beams are coupled to the apparatus head in a single polarization-maintaining single-mode fiber and then passed through a quarter wave plate ($\lambda/4$) before and after the atoms. This is followed by the inertial reference retroreflector. The orientation of Bragg optics is such that the Bragg transitions are driven by circularly polarized light. One beam is frequency chirped to match the increasing doppler shift of the atoms as they fall, while the other is adjusted to address the resonance frequency for transfer of $2\hbar k$ of momentum, where k is the wave number of the light. The Bragg laser is aligned to vertical using a liquid mercury mirror and back

coupled into the output fiber over a 6 m total path length. A homebuilt external cavity diode laser seeds a frequency doubled 1560 nm fiber laser system capable of producing 11 W of 780 nm light with a linewidth of 5 kHz, generating the Bragg and Raman light [27]. Independent frequency control and pulse shaping for all Bragg and Raman beams is accomplished using four acousto-optic modulators driven with a direct digital synthesizer and referenced to a cesium primary frequency standard. No active optical phase locking systems have been implemented in the current setup.

A 5 cm gold mirror mounted on a homebuilt geometric antispring (GAS) [28] provides the inertial reference. The GAS provides passive filtering of ground vibrations by virtue of a low frequency mechanical oscillator. This passive oscillator is tuned to an ultralow natural frequency of 180 mHz. A direct measurement of the GAS transfer function shows significant isolation from 1 Hz (< -22 dB) and greater (< -76 dB at 70 Hz).

The various experimental cycles and the data acquisition are as follows. A BEC of 2×10^6 atoms is created and released into free fall. After 5 ms of free fall the atoms are either left in the initial m_f state or transferred into a superposition of 25% $|m_f = -1\rangle$, 50% $|m_f = 0\rangle$, and 25% $|m_f = 1\rangle$; see Fig. 2(c). The time between the cloud release and the start of the interferometer, T_0, is varied from 7 to 100 ms to investigate the effect of undissipated mean-field energy on the phase noise of the interferometer; see Fig. 3. This phase noise is seen to be correlated to cloud density variations due to imperfect beam splitter pulses and asymptotes at $T_0 \approx 20$ ms. This behavior follows a simple mean-field model of energy [21] and corresponds to $\sim$1 mrad of additional phase noise at $T_0 \approx 20$ ms.

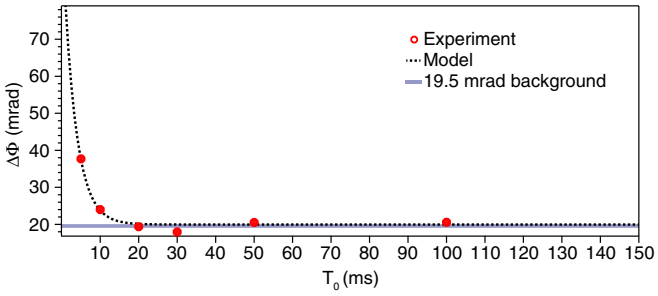

FIG. 3. A pure BEC source is allowed to expand for various times, T_0, before a $T = 60$ ms Mach-Zehnder interferometer is performed. The efficiency of the first beam splitter pulse is varied by up to 15%, ensuring different atom numbers in each arm. This number imbalance will lead to a relative phase shift on the arms due to mean-field interactions. By performing many runs, the phase noise from this number imbalance and initial cloud density can be found. The phase noise from mean-field effects in this system asymptote at 20 ms to the background phase noise from the Bragg laser system. A basic mean-field model of the system is plotted against this data with good agreement.

Because of this effect, 30 ms of free expansion is allowed for all high sensitivity interferometers.

Following free expansion, a sequence of Gaussian shaped Bragg pulses of 50 μs full width half maximum are applied to form a Mach-Zehnder interferometer. By scanning the phase of the final beam splitter, an interference fringe can be produced [Fig. 2(g)]. The time between interferometer pulses, T, may be varied from 1 to 250 ms. By scanning T in a magnetically sensitive interferometer, the fringe contrast is explored in regions of varying cloud separation at the final beam splitter; see Fig. 4. The curvature of the magnetic field along the 2.5 m drop leads to unequal accelerations felt by each interferometer arm. This asymmetric acceleration results in a final positional separation of the two arms at the final beam splitter pulse. The total separation is proportional to T^2. A BEC source is shown to maintain contrast ($\approx$80%) over the full interferometer range, suggesting that the coherence length of a BEC ensures a robustness to the systematics leading to a mismatch at the final beam splitter. By comparison, a thermal cloud (velocity selected to 90 nK) undergoing the same experimental sequence exhibits a 7% contrast at $T = 40$ ms. Following the final beam splitter pulse, a variable amplitude magnetic field gradient from a vertical coaxial solenoid can be applied to impart Stern-Gerlach separation of the different magnetic states (Fig. 2). The $2\hbar k$ momentum separation of the interferometer arms requires 200 ms of free propagation for sufficient separation of the final momentum states. Large momentum transfer beam splitters would alleviate the need for this long separation time [29]. Finally, the number of atoms in each momentum and the internal state is measured using FMI. The total phase shift accumulated in each interferometer is given by $\phi_{\text{total}} = \phi_g + \phi_B$, where ϕ_g and ϕ_B are given by

$$\phi_g = n k_{\text{eff}} g T^2$$
$$\phi_B = \frac{n k_{\text{eff}} T^2}{m_{\text{Rb}}} \frac{\partial B}{\partial z} \mu_B \left[g_I m_f \pm \frac{(g_J - g_I)}{4\sqrt{A}} (m_f + 2x) \right]. \quad (1)$$

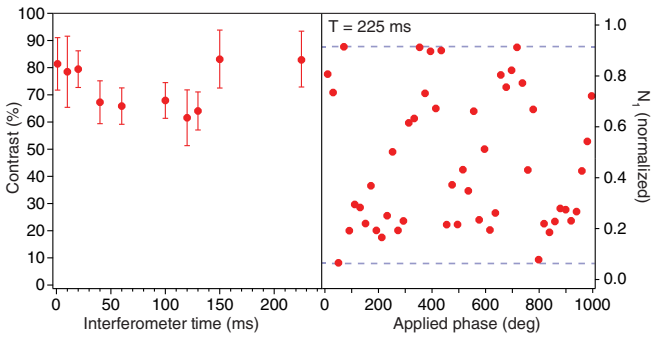

FIG. 4. The contrast of an $|m_f = -1\rangle$ BEC interferometer for various T's. Contrast is defined here as the difference between the maximum and the minimum of an interference fringe.

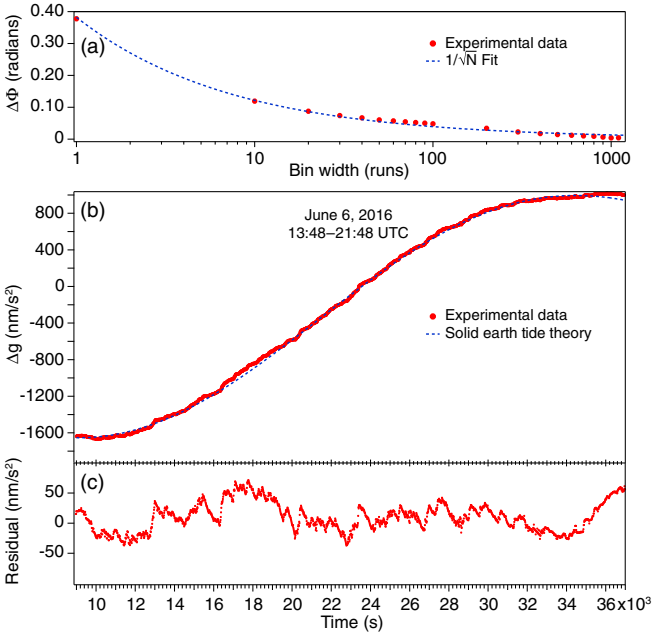

FIG. 5. The deviation in gravitational acceleration over an 8 h period is monitored using a spinor BEC sourced $T = 130$ ms interferometer. Data corresponding to the $|m_f = 0\rangle$ state is plotted. (a) The integrated phase sensitivity of the interferometer corresponding to varying bin widths (circles) shown with a $1/\sqrt{N}$ fit (dashed line). A maximum phase sensitivity of 3.8 mrad is reached for a 1000 run bin width. (b) 1000 point running average of experimental data (circles) with the solid Earth tide theory overlaid (dashed line). (c) The residual of the experimental data and the solid Earth tide theory. A maximum precision of $\Delta g/g = 8 \times 10^{-8}$ per run and $\Delta g/g = 1.45 \times 10^{-9}$ in 1000 runs was achieved.

ϕ_B is derived from the Breit-Rabi formula where $A = 1 + m_f x + x^2$, with $x = (g_J - g_I)\mu_B B/\Delta E_{hfs}$. A typical three state FMI interferometer signal and scanned fringe is shown in Fig. 2(g).

A $T = 130$ ms spinor BEC interferometer was run continuously over an 8 h period on June 6, 2016, monitoring deviations in gravitational acceleration from the solid Earth tides. The integrated phase sensitivity of the apparatus follows the expected $1/\sqrt{N}$ scaling, where N is the number of binned points [Fig. 5(a)]. At $N = 1000$, the sensitivity asymptotes to 3.8 mrad. Figure 5(b) shows the experimental data with a 1000 point running average overlaid with the theoretical solid Earth tide. The residual of the experimental data and solid Earth tide theory is shown in Fig. 5(c). The achieved gravitational acceleration sensitivity of this device reached a combined three state precision of $\Delta g/g = 8 \times 10^{-8}$ per run and $\Delta g/g = 1.45 \times 10^{-9}$ in 1000 runs. This sensitivity is limited by laser phase noise on the passive Bragg laser system.

As seen in Eq. (1) and Fig. 2, the interferometers in the $|m_f = -1\rangle$ and $|m_f = 1\rangle$ states are phase shifted with opposite signs away from the magnetically insensitive $|m_f = 0\rangle$ state. By comparing the relative phase shifts, the three fringes can be combined to extract the absolute magnetic field gradient, the absolute magnetic field, and local gravity. In addition, it is straightforward to extend the system to measure gravity gradients [22].

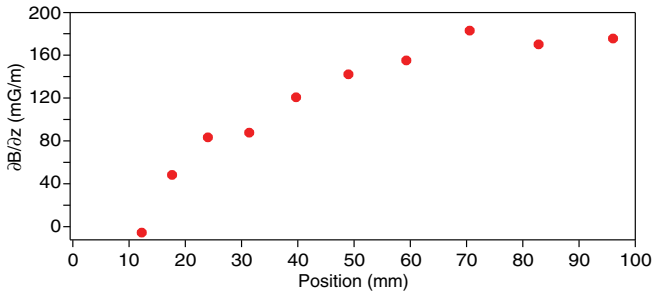

FIG. 6. The magnetic field gradient along a portion of the drop-in mapped by varying the initial position of a $T = 40$ ms interferometer, where the initial cloud has been prepared in a superposition of $|m_f = -1\rangle$ and $|m_f = 1\rangle$. The error in gradient measurement is less than the point size.

Figure 6 shows the measure of the magnetic field gradient along a portion of the drop. The maximum achieved phase sensitivity enables an absolute magnetic field gradient sensitivity of 120 pT/m. To date, this is the highest achieved atom-based magnetic gradient sensitivity. This is competitive with state-of-the-art relative devices such as solid-state (0.52 nT/m, 1 s integration) [30] and SQUID-based systems (10 pT/m, 1 s integration) [31]. A more sophisticated analysis of the sensor noise is likely to achieve significantly higher precision through common mode noise reduction. At current precision, this sensor is capable of recognizing weak magnetic features such as paramagnetic rock anomalies at depths of 1 km [7]. This step change in sensor technology enabled by fundamental properties in source selection will allow for the simultaneous precision exploration of gravitational and magnetic anomalies leading to higher spatial resolution mapping, as well as the ability to differentiate the feature's material properties.

In conclusion, a high precision simultaneous gravimeter, magnetic gradiometer, and magnetometer based on a free falling Bose-condensed source was demonstrated. The atomic source provides internal degrees of freedom, allowing for the preparation of magnetically sensitive states. Because of the large and spatially varying background magnetic field of the surrounding environment, the simultaneous measurement of all states (magnetic and nonmagnetic) would not be possible without the macroscopic spatial coherence provided by the condensed source. The flexibility of this device allowed for direct mean-field noise characterization of a BEC in a high precision apparatus. Furthermore, a direct comparison of thermal and BEC sources was achieved, showing that, under near

identical systematic conditions, a condensate has contrast a factor of 5 higher than the thermal cloud. A full noise characterization of the system will be investigated in the future. This is the first iteration towards an all-in-one quantum sensor which will be capable of simultaneous measurement of g, Δg, B, ΔB, rotations, and time. Currently, work is ongoing to implement symmetric horizontal Bragg transitions to also measure rotations.

A technical hurdle that needs to be overcome for condensed sources to become viable in field deployable devices is the time required to prepare a large BEC (10 s). Significant progress towards solving this problem was reported and summarized recently [32]. Nonetheless, fast condensate production generally sacrifices the total atom number for the duty cycle. This is evident from the best integrated flux [32] achieved in fast devices, 2.5×10^5 atoms/s, when compared to the 4×10^5 atoms/s flux in this device. Applications of techniques such as sideband cooling offer a path for improving flux on both atom chip and free-space-based sensors [33] without sacrificing atom number. The possibility of integrating sideband cooling techniques with the current sensor is being explored.

*kyle.hardman@anu.edu.au, http://atomlaser.anu.edu.au/

[1] CSEG Rec. **35**, 30 (2010).
[2] D. B. Hoover, D. P. Klein, and D. C. Campbell, Report No. 95-831, U.S. Geological Survey, 1996.
[3] A. DeGregoria, Ph.D. thesis, Air Force Institute of Technology, 2010.
[4] J. L. Chen, C. R. Wilson, and B. D. Tapley, Science **313**, 1958 (2006).
[5] L. Lacoste, N. Clarkson, and G. Hamilton, Geophysics **32**, 99 (1967).
[6] I. Marson and J. E. Faller, J. Phys. E **19**, 22 (1986).
[7] J. M. Merayo, P. Brauer, and F. Primdahl, Sens. Actuators A **120**, 71 (2005).
[8] J. M. Goodkind, Rev. Sci. Instrum. **70**, 4131 (1999).
[9] A. Peters, K. Y. Chung, and S. Chu, Metrologia **38**, 25 (2001).
[10] J. M. McGuirk, G. T. Foster, J. B. Fixler, M. J. Snadden, and M. A. Kasevich, Phys. Rev. A **65**, 033608 (2002).
[11] H. Müller, S.-w. Chiow, S. Herrmann, S. Chu, and K.-Y. Chung, Phys. Rev. Lett. **100**, 031101 (2008).
[12] J. Le Gouët, T. Mehlstäubler, J. Kim, S. Merlet, A. Clairon, A. Landragin, and F. Pereira Dos Santos, Appl. Phys. B **92**, 133 (2008).
[13] R. Geiger, V. Ménoret, G. Stern, N. Zahzam, P. Cheinet, B. Battelier, A. Villing, F. Moron, M. Lours, Y. Bidel *et al.*, Nat. Commun. **2**, 474 (2011).
[14] Z.-K. Hu, B.-L. Sun, X.-C. Duan, M.-K. Zhou, L.-L. Chen, S. Zhan, Q.-Z. Zhang, and J. Luo, Phys. Rev. A **88**, 043610 (2013).
[15] B. Altschul, Q. G. Bailey, L. Blanchet, K. Bongs, P. Bouyer, L. Cacciapuoti, S. Capozziello, N. Gaaloul, D. Giulini, J. Hartwig *et al.*, Adv. Space Res. **55**, 501 (2015).
[16] http://www.muquans.com/index.php/products/aqg (2016).
[17] http://www.atomsensors.com/index.php/en/ (2016).
[18] http://aosense.com (2016).
[19] M. Schmidt, A. Senger, M. Hauth, C. Freier, V. Schkolnik, and A. Peters, Gyroscopy Navig. **2**, 170 (2011).
[20] K. S. Hardman, C. C. N. Kuhn, G. D. McDonald, J. E. Debs, S. Bennetts, J. D. Close, and N. P. Robins, Phys. Rev. A **89**, 023626 (2014).
[21] J. E. Debs, P. A. Altin, T. H. Barter, D. Döring, G. R. Dennis, G. McDonald, R. P. Anderson, J. D. Close, and N. P. Robins, Phys. Rev. A **84**, 033610 (2011).
[22] P. A. Altin, M. T. Johnsson, V. Negnevitsky, G. R. Dennis, R. P. Anderson, J. E. Debs, S. S. Szigeti, K. S. Hardman, S. Bennetts, G. D. McDonald *et al.*, New J. Phys. **15**, 023009 (2013).
[23] I. Bloch, T. W. Hansch, and T. Esslinger, Nature (London) **403**, 166 (2000).
[24] S. S. Szigeti, J. E. Debs, J. J. Hope, N. P. Robins, and J. D. Close, New J. Phys. **14**, 023009 (2012).
[25] G. C. Bjorklund, M. D. Levenson, W. Lenth, and C. Ortiz, Appl. Phys. B **32**, 145 (1983).
[26] K. S. Hardman, P. B. Wigley, P. J. Everitt, P. Manju, C. C. N. Kuhn, and N. P. Robins, Opt. Lett. **41**, 2505 (2016).
[27] S. S. Sané, S. Bennetts, J. E. Debs, C. C. N. Kuhn, G. D. McDonald, P. A. Altin, J. D. Close, and N. P. Robins, Opt. Express **20**, 8915 (2012).
[28] G. Cella, V. Sannibale, R. DeSalvo, S. Márka, and A. Takamori, Nucl. Instrum. Methods Phys. Res., Sect. A **540**, 502 (2005).
[29] G. D. McDonald, C. C. N. Kuhn, S. Bennetts, J. E. Debs, K. S. Hardman, M. Johnsson, J. D. Close, and N. P. Robins, Phys. Rev. A **88**, 053620 (2013).
[30] Y. Sui, G. Li, S. Wang, and J. Lin, Rev. Sci. Instrum. **85**, 014701 (2014).
[31] S. T. Keenan, J. A. Young, C. P. Foley, and J. Du, Supercond. Sci. Technol. **23**, 025029 (2010).
[32] J. Rudolph, W. Herr, C. Grzeschik, T. Sternke, A. Grote, M. Popp, D. Becker, H. Müntinga, H. Ahlers, A. Peters *et al.*, New J. Phys. **17**, 065001 (2015).
[33] X. Li, T. A. Corcovilos, Y. Wang, and D. S. Weiss, Phys. Rev. Lett. **108**, 103001 (2012).